Remote Sensing of Environment 199 (2017) 321–332

Contents lists available at ScienceDirect

Remote Sensing of Environment

journal homepage: www.elsevier.com/locate/rse

Snow thickness estimation on first-year sea ice using microwave and optical remote sensing with melt modelling

Jiacheng Zheng, Torsten Geldsetzer, John Yackel *

Cryosphere Climate Research Group, Dept. of Geography, University of Calgary, Calgary, Alberta, Canada

ARTICLE INFO

Article history:
Received 6 January 2017
Received in revised form 26 May 2017
Accepted 28 June 2017
Available online 1 August 2017

Keywords:
Snow
Sea ice
Microwave scattering
Melt onset
Albedo
Melt ponds
Melt modelling

ABSTRACT

The snow cover on first-year sea ice plays a paramount role in thermodynamics by modulating sea ice ablation and accretion processes. However, meteoric accumulation and redistribution of snow on first-year sea ice is highly stochastic over space and time, which makes it a poorly understood parameter. In this study, a region of late-winter snow thickness on first-year sea ice in the Canadian Arctic Archipelago is estimated using time series spaceborne C-band microwave scatterometer and optical MODIS data and a simple snow melt model. Results show good correspondence between the modeled snow thickness and remotely sensed dates of melt onset and pond onset. The mean snowmelt duration for 20 study sites is 24.6 ± 1.2 days, and the estimated mean snow thickness is 14.7 ± 3.0 cm. The overall performance of the model reveals a RMSE of 4.0 cm and a mean bias of 0.3 cm. The methodology shows promise; particularly because it can easily be scaled up in order to estimate snow thickness on seasonal sea ice on a regional basis.

1. Introduction

One of the primary shortcomings in Global Climate Models is the inaccurate parameterization of snow covered sea ice in the polar regions. Arctic sea ice is very sensitive to temperature changes, and even small variations in temperature may trigger large effects within the climate system (IPCC, 2013). One of the most dramatic changes is the rapid reduction of multi-year sea ice (MYI) in recent years (Maslanik et al., 2007; Kwok and Rothrock, 2009). First-year sea ice (FYI), which accretes and ablates annually, continues to occupy these regions of the Arctic Ocean previously covered by MYI. These changes in MYI and FYI proportion are occurring during an overall decline of Arctic sea ice area and thickness (Lindsay and Schweiger, 2015) and are expected to impact the entire Arctic including atmospheric, oceanographic, ecological, and socio-economic systems (Post et al., 2013).

Snow cover on FYI plays a key role in sea ice thermodynamic processes (Brown and Cote, 1992; Iacozza and Barber, 2010; Webster et al., 2014; Maass et al., 2015) by modulating sea ice accretion and ablation processes. During winter, the growth of sea ice is limited due to the strong insulating properties of snow. In summer, the high albedo snow cover acts to retard sea ice melt by reflecting shortwave radiation potentially available for warming the sea ice. Due to its high albedo and low thermal conductivity, the snow cover plays a key role in the positive feedback loop initiated by atmospheric warming (Maass et al., 2015). As a result, the warmer ocean will further contribute to sea ice thickness reductions from bottom ice melt (Eicken and Lemke, 2001) and delayed sea ice freeze-up in fall. These processes will lead to an even greater warming of the atmosphere (Moritz et al., 2002), due to enhanced evaporation and an increase to the atmospheric moisture flux, leading to a potential increase in meteoric precipitation to some regions of the marginal sea ice zone.

Meteoric accumulation and redistribution of the snow cover on FYI is highly stochastic over space and time and is generally poorly understood (Iacozza and Barber, 1999; Iacozza and Barber, 2010). An initial step towards understanding snow thickness distributions is to measure the magnitude of the snow thickness both spatially and temporally (Barber et al., 1998; Yackel et al., 2007). Previous studies show that the information about snow cover on FYI can be measured through in-situ based (e.g. Iacozza and Barber, 1999), laboratory based (e.g. Lytle et al., 1993), and remote sensing based techniques (e.g.; Barber et al., 1998; Markus et al., 2006; Yackel et al., 2007; Yackel and Barber, 2007; Kurtz et al., 2013). Owing to the logistical difficulty of direct measurement, a reliance on remote sensing techniques is required (Sturm et al., 2002; Nandan et al., 2016).

Spaceborne optical remote sensing data provide surface reflectance information (i.e. albedo) regarding snow covered FYI with a relatively fine spatial (e.g. 250 m) and temporal resolution (e.g. daily) (Hall et al., 2005). Active microwave remote sensing provides all-weather,

* Corresponding author at: Cryosphere Climate Research Group, Department of Geography, University of Calgary, 2500 University Dr NW, Calgary, AB T2N 1N4, Canada.
E-mail address: yackel@ucalgary.ca (J. Yackel).

http://dx.doi.org/10.1016/j.rse.2017.06.038
0034-4257/

high spatial resolution data and has demonstrated capability to characterize the seasonally evolving thermodynamic state of snow covered FYI (Livingstone et al., 1987; Barber et al., 1994).

2. Background

2.1. Seasonal evolution of snow covered FYI

The seasonal evolution of snow covered Arctic FYI is categorized into thermodynamic regimes based on the average processes operating within the system during the annual cycle (Barber et al., 1994). The categories include *freeze-up*, *winter*, *early melt*, *melt onset* and *advanced melt*. The initial freezing of Arctic seawater marks beginning of *freeze-up*, which generally occurs in October and November due to decreasing solar radiation and surface air temperature (Maykut and Untersteiner, 1971). As solar radiation and surface air temperature continue to decrease, the thin sea ice grows thicker and a layer of snow begins to accumulate on its surface. *Winter* generally occurs from December to April, and FYI typically accumulates an increasingly thicker snow cover due to cold temperatures and precipitation throughout the winter from the passage of periodic synoptic scale cyclones, which also causes significant snow redistribution (Iacozza and Barber, 2010). In late April or May, the *early melt* stage begins as snow temperature increases with increasing solar input, and the diurnal temperature range in the snow cover increases. *Melt onset* occurs in May or June when liquid water begins to accumulate near the top of the snow cover and among the interstices of the snow grains within the snow volume (Barber et al., 1994). With continued warming above 0 °C, snow water volume increases to the point where the gravity bonds break and the water drains freely to the base of the snow cover (pendular to funicular transition) (Colbeck, 1983; Barber et al., 1995). As snow continues to melt, ponds begins to appear (*pond onset*) on the FYI surface and the *advanced melt* stage begins. During this stage, a dynamic mosaic of melt ponds, bare ice and snow patches characterizes the FYI surface (Maykut and Untersteiner, 1971; Holt and Digby, 1985). As summer progresses, the ponds drain through FYI as the ice continues to melt and decay, often aided by strong winds until the sea ice breaks up and open water prevails (Hanesiak et al., 2001; Eicken et al., 2002; Eicken et al., 2004).

2.2. Backscatter and albedo interactions with seasonally evolving snow covered FYI

Active microwave interactions with snow covered FYI are a function of snow and ice electro-thermo-physical properties (Barber et al., 1998; Barber and Nghiem, 1999). The temporal evolution of the microwave backscatter coefficient (sigma nought - σ°) illustrates that a significant amount of information regarding the thermodynamic characteristics of seasonally evolving snow-covered FYI can be deduced (Barber et al., 1994; Barber et al., 1995; Grenfell et al., 1998). During *winter* and *early melt*, σ° from FYI is low and stable (Fig. 1). Smoother FYI produces a lower σ° than rougher forms of FYI, regardless of frequency (Ulaby et al., 1984). σ° occasionally oscillates during *winter* in accordance with changes in the atmospheric heat flux which causes an increase in volume scattering from the high dielectric basal snow layer which has elevated brine volume (Livingstone and Drinkwater, 1991; Barber et al., 1995; Barber and Thomas, 1998; Barber and Nghiem, 1999; Yackel and Barber, 2007). The combination of the ice surface micro- and macroscale roughness, snow grain size and brine volume (as a function of temperature and salinity) determines the overall magnitude of scattering (Barber and Nghiem, 1999).

Early melt begins when the snow volume temperature approaches −5 °C causing a rapid increase in brine volume in the basal snow layer during the warmer portion of the diurnal cycle. This causes an increase to the dielectric constant, which contributes to an increase in volume scattering (Drinkwater and Crocker, 1988; Barber et al., 1994; Golden et al., 1998). A large diurnal range in backscatter is characteristic of this period owing to the increasing diurnal range in air and snow volume temperatures (Yackel and Barber, 2007).

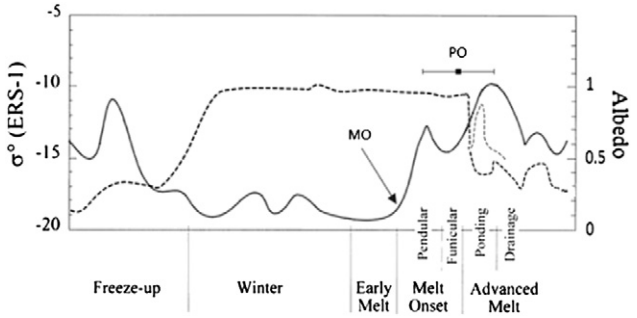

Fig. 1. Phenomenological seasonal evolution of the microwave backscatter coefficient (σ°) from C-band SAR and satellite-estimated albedo from MODIS for snow covered FYI over the seasonal periods spanning the annual cycle. The solid curve represents backscatter, and the dashed curve represents albedo. Generally, MO (melt onset) occurs at the same time for snow cover with different snow thickness; on the other hand, PO (pond onset) varies depending on snow thickness. The theoretically error bar of PO on the figure marks the timing of PO for thin and thick snow cover. The light grey dashed line depicts the albedo change for shallow pond drainage, or overnight pond refreezing, and/or snow on frozen pond during PO. (Adapted from Livingstone et al., 1987; Barber et al., 1995; Yackel et al., 2007.)

Melt onset is denoted by a sharp increase in σ° (Fig. 1), due to increasing surface and volume scattering resulting from a continued increase in liquid water content (Livingstone and Drinkwater, 1991; Barber et al., 1995). When snow cover thickness on FYI is sufficient (typically >30 cm), there is a distinct dip in σ° corresponding with the transition from the pendular to funicular snow regimes (Colbeck, 1982; Barber et al., 1995; Yackel et al., 2007). This gravity related process marks a reduction of liquid water in the top snow layers coincident with an increase in liquid water at the base of the snow cover (Barber et al., 1995). This liquid water drainage within the snow cover during the funicular regime leads to reductions in both snow surface and volume scattering. The pendular regime appears absent when snow thickness is ≲10 cm (Yackel et al., 2007).

During *advanced melt*, σ° remains high over the ponding period as the overall liquid water content on the surface remains high. Melt pond surface scattering increases when wind roughened (Barber and Yackel, 1999; Yackel and Barber, 2000; Scharien et al., 2014). σ° decreases when the ponds drain through the ice leaving a lower dielectric snow and ice patch mosaic.

Similar to microwave backscatter, the presence of liquid water within the snow cover dominates the optical reflectance and albedo of FYI (Barber and LeDrew, 1994). Snow albedo is largely dependent on grain size, and decreases at all wavelengths as the grain size increases, because larger grains are both more absorptive and forward scattering than smaller grains (Wiscombe and Warren, 1980). When liquid water in the snow cover increases, it replaces air between the ice grains (Colbeck et al., 1975; Colbeck, 1979). Since the spectral refractive index of liquid water is very close to that of ice (~5 μm), this replacement of air by water between ice grains can increase the effective grain size (Irvine and Pollack, 1968). Therefore, spectral albedo exhibits a general decrease for all wavelengths as liquid water content increases, which continues as the melt season progresses (Grenfell and Perovich, 2004).

The albedo of cold, dry snow on FYI during winter is high and stable (Fig. 1). Once the snow cover is >3 cm, the albedo of FYI can be as high as 0.95, especially for the case of freshly fallen meteoric snow (Brandt et al., 2005). When the snow temperature approaches 0 °C, ice grains/crystals transition to liquid water which initiates a rapid decreases the albedo, signifying *melt onset* (Perovich and Polashenski, 2012) (Fig. 1). A rapid and significant decrease in surface albedo occurs at the beginning of *advanced melt* as melt ponds begin to form on the surface. The albedo may increase temporarily if the ponds freeze over and provide a temporary platform for snow accumulation. Albedo thereafter fluctuates until sea

ice break up as the surface mosaic of melt ponds (low albedo), drained melt ponds and drained ice (higher albedo) fraction varies owing to hydraulic controls on sea ice freeboard (Eicken et al., 2004) (Fig. 1).

2.3. Snow-melt modelling

There are two fundamental types of snow melt models for daily or shorter time steps; namely, energy balance and temperature-index approaches. Energy balance approaches attempt to quantify each term in the energy balance equation and simulate the energy fluxes within the snowpack (Hock, 2003). However, this method is very data intensive and as a result not often employed. An alternative is the temperature-index approach, with the most common of these being the degree-day model, based on the assumption of an empirical relationship between air temperature and melt rate (Hock, 2003). The degree-day model has been widely used and refined over the past 80 years (e.g. Clyde, 1931; Collins, 1934; Hoinkes and Steinacker, 1975; Kustas et al., 1994; Rango and Martinec, 1995; Kane et al., 1997). The degree-day model maintains its popularity due to limited data (air temperature only) requirements and has provided consistent model performance (e.g. Rango and Martinec, 1995; Hock, 2003) while remaining computationally simplistic (Kustas et al., 1994). A major limitation of this model, once initiated, is that it is not able to account for cooling in the snowpack when the temperature gets below 0 °C (Kuusisto, 1984).

Since the degree-day model relies on the relationship between air temperature and melting rate, the model works well only when a strong correlation is between air temperature and the energy flux responsible for melt (Kane et al., 1997). This model requires two site-specific coefficients including a threshold air temperature offset and a melt coefficient (also referred to as the degree-day factor, DDF). The values of the threshold temperature are usually below 0 °C because some ablation can occur through radiative melt even when the air temperature is below freezing. The temperature offset used in this study is lower than regular snowmelt temperatures (i.e. −0.2 °C in Kane et al., 1997), because a microwave approach is able to detect snowmelt earlier due to the sensitivity of microwaves to detect infinitesimal amounts of water in or on the surface of the snow cover. For the melt coefficient, results from previous studies reveal large variability from site to site. Reported melt coefficients are mostly from glaciers and snow-covered basins on land, and only Iacozza and Barber (2001) have investigated snowmelt rates on FYI but deriving a melt coefficient was not an objective of their work. Generally, direct measurements (e.g. Kustas et al., 1994; Braithwaite et al., 1998) and melt obtained by energy balance computations (e.g. Arendt and Sharp, 1999) are the two ways of computing melt coefficients. In addition, values of melt coefficients might be sensitive to the temporal average that are used (Arnold and Mackay, 1964); when temperature fluctuates around the freezing point, using daily mean temperature could be misleading, resulting in overestimated melt coefficients (Hock, 2003). We calibrate the melt coefficient for our snow covered FYI site using in-situ observations including snow depth and melt duration. Hourly on-ice measured air temperature is used to run the model.

3. Objectives

In this study, time series daily observations of active microwave [Advanced SCATterometer (ASCAT)] and optical [MODerate-resolution Imaging Spectroradiometer (MODIS)] satellite data are used in conjunction with in situ acquired meteorological data and a simple snow melt model for the purpose of modelling late winter snow thickness on FYI. The following research questions towards this objective are stated.

(1) Can we detect melt-onset (MO) for snow covered FYI using time series microwave backscatter from ASCAT?
(2) Can we detect pond-onset (PO) for snow covered FYI using time series optical albedo from MODIS MCD43A?
(3) What calibration is required for the degree-day factor (melt coefficient) in the snowmelt model for snow covered FYI using in-situ measurements?
(4) Can we estimate the winter (pre-melt onset) snow thickness distribution using the answers from questions 1–3 above together with meteorological data?

4. Methods

4.1. Study area

The region under investigation is snow covered landfast FYI in Dease Strait near Cambridge Bay, Nunavut, Canada (Fig. 2). Twenty (20) study sites were pre-selected prior to the start of the study, which span the range of FYI surface roughness conditions (as assessed from RADARSAT-2 SAR) within Dease Strait. All of the sites were located sufficiently far away (minimum of 5 km) from coastlines to avoid possible land contamination within the satellite data. All of the in-situ snow measurements acquired for validation in this study were collected during the Ice Covered Ecosystem-Cambridge Bay Process Studies (ICE-CAMPS; http://umanitoba.ca/faculties/environment/departments/ceos/research/1197.html) field campaign, 2014.

4.2. Data

4.2.1. ASCAT

ASCAT is an active microwave advanced scatterometer on the polar-orbiting European Organisation for the Exploitation of Meteorological Satellites (EUMETSAT) satellites: MetOp-A and MetOp-B, launched in 2006 and 2012, respectively. ASCAT is a real aperture radar, transmitting pulses in vertical co-polarization (VV) and operating in C-band at 5.255 GHz. It has two sets of three fan-beam antennae measuring the returned backscatter signal at incident angles between 25° and 65°. The antennae extend on either side of the instrument, which results in a double swath of observations, each 550 km wide, separated by a gap of approximately 360 km (Figa-Saldaña et al., 2002). ASCAT provides a daily, 80% global imaging coverage, and is capable for 'all-condition' surface measurements due to its efficient penetration of atmosphere and clouds, and independence of solar illumination (Mortin et al., 2014).

The ASCAT standard backscatter product has nominal spatial resolution of 25 or 50 km with very high temporal resolution (multiple passes per day). However, to achieve the small-scale investigation in this study, a resolution-enhanced product provided by Brigham Young University (BYU) Microwave Earth Remote Sensing (MERS) Laboratory is utilized (Lindsley and Long, 2010). We use the Scatterometer Image Reconstruction (SIR) 4.45 km resolution all-passes product, which is a composite of several overpasses made over the pole during a day (Early and Long, 2001; Lindsley and Long, 2010; Long et al., 1993). SIR has been applied to several microwave instruments and is distributed by the Scatterometer Climate Record Pathfinder project (Mortin et al., 2014). The temporal resolution of the SIR data is sufficient for studying the seasonal transitions of snow cover on FYI (Howell et al., 2006; Mortin et al., 2014). The original SIR product is normalized to 40° incidence angle using daily estimates of incidence angle dependence (Long et al., 1993). We normalize the SIR data to a consistent incidence angle of 49° (details are provided in section 4.5). A consistent incidence angle is needed to address daily-time scale thermodynamic changes to the snow and ice surface physical properties, which in turn change the dielectric properties ultimately manifesting as a change in backscatter. As such, we expect scatterometer backscatter quantities, due to changes in incidence angle, to be negligible and to be solely from snow and sea ice thermodynamically driven physical property changes (Mahmud et al., 2016).

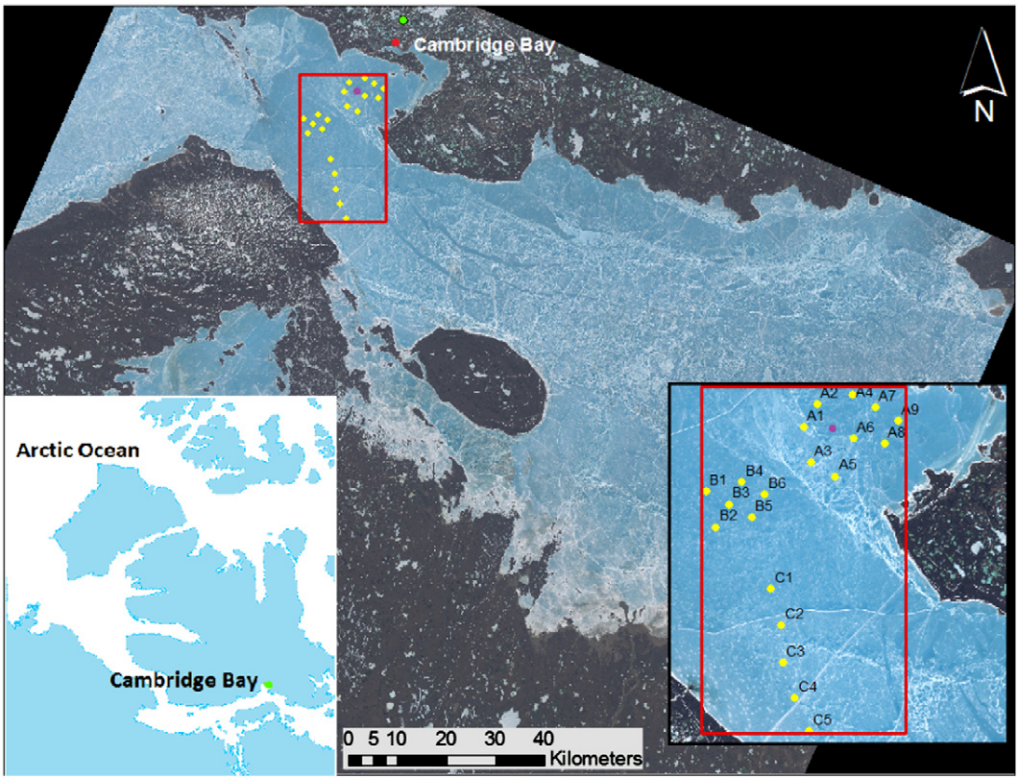

Fig. 2. Study area map indicating the location of the 20 sample site locations on snow covered smooth first-year sea ice within Dease Strait near Cambridge Bay, NU. The background image is a Landsat 8 band 3, 2 and 1 true colour composite acquired on June 22, 2014. The Cambridge Bay Township is marked by a green dot, the airport weather station is marked by a red dot, and the on-site micro-meteorological station is marked by a purple dot on the maps.

4.3. MODIS albedo product (MCD43A3)

We use the MODIS MCD43A3 product, which combines data acquired from the Moderate Resolution Imaging Spectroradiometer launched on both Terra and Aqua satellites by NASA in 1999 and 2002, respectively. The standard MCD43A3 product includes the weighting parameters that are associated with a bi-directional reflectance distribution function (BRDF) model and describes the reflectance anisotropy of each pixel in the image (Lucht et al., 2000; Schaaf et al., 2002). 16 days of clear sky, multi-angle high quality surface reflectance from both Terra and Aqua are used to obtain sufficient angularly well-distributed observations to fit the BRDF model (Gao et al., 2001; Roy et al., 2006; Wanner et al., 1997). The BRDF model utilizes the weighted sum of isotropic, volumetric and geometric parameters to describe the reflectance anisotropy (Schaaf et al., 2002).

In this study, we use the MODIS BRDF/albedo V006 daily product provided by Boston University. This MCD43A3 product operates in a daily rolling mode to provide more frequent surface albedos than the current standard product (Wang et al., 2012). It has a spatial resolution of 250 m, designed to capture rapid surface changes including regional vegetation phenology and snow melt. The MODIS daily retrieval uses a moving window of the surrounding 16-days observations and strongly emphasizes the day of interest (center date of the 16 days) with higher weights during the retrieval. Surface albedo is derived by integrating the hemisphere BRDF model. A magnitude inversion for each day and the full inversions from the 16-day daily mode is used as the a priori information for the next day (Zhuosen et al., 2012). Several studies have shown that, in general, the magnitude inversion can perform well under most situations (Jin et al., 2003a, b; Liu et al., 2009; Salomon et al., 2006). The MODIS product provides four bands, including a visible (620–670 nm) and a near-infrared (841–876 nm) band for both bi-hemispherical reflectance (white-sky albedo, WSA) and directional–hemispherical reflectance (black-sky albedo, BSA) at local solar noon. We selected the visible band for WSA in this study due to snow having a stronger spectral response in the visible compared to the near infrared. We note that the WSA has the angular dependency removed.

4.4. In-situ snow depth measurements

Snow depth measurements for 20 study sites in Dease Strait were acquired on April 19, 20, and 22, 2014 (Table 1; Fig. 2). Snow depth at each site was measured using a hand ruler, and sampling was

Table 1
Study sites locations, snow thickness and dates of measurements.

Site ID	Date	Snow thickness ± stdev (cm)	Longitude	Latitude
A1	19/04/2014	16.1 ± 10.9	−105.415	69.027
A2	19/04/2014	14.5 ± 5.9	−105.388	69.045
A3	19/04/2014	12.3 ± 5.4	−105.394	69.0007
A4	19/04/2014	15.0 ± 4.9	−105.311	69.0525
A5	19/04/2014	13.1 ± 8.0	−105.346	68.990
A6	19/04/2014	14.6 ± 6.2	−105.291	69.025
A7	19/04/2014	12.5 ± 4.8	−105.264	69.042
A8	19/04/2014	13.9 ± 6.2	−105.242	69.015
A9	19/04/2014	14.7 ± 5.6	−105.215	69.0328
B1	20/04/2014	13.6 ± 4.9	−105.621	68.9781
B2	20/04/2014	14.8 ± 8.3	−105.599	68.951
B3	20/04/2014	12.2 ± 4.6	−105.573	68.968
B4	20/04/2014	14.2 ± 5.9	−105.545	68.985
B5	20/04/2014	15.3 ± 6.5	−105.524	68.958
B6	20/04/2014	18.0 ± 7.4	−105.497	68.9759
C1	22/04/2014	17.8 ± 8.2	−105.483	68.904
C2	22/04/2014	15.4 ± 6.1	−105.462	68.877
C3	22/04/2014	14.1 ± 8.0	−105.441	68.8502
C4	22/04/2014	14.5 ± 8.1	−105.420	68.823
C5	22/04/2014	12.6 ± 7.3	−105.400	68.796

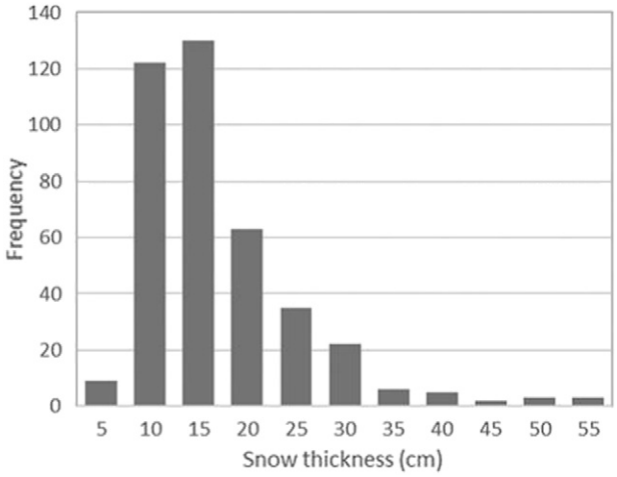

Fig. 3. Example of snow thickness distribution at field site B2: 2014-04-20, n = 400.

conducted in an "L" shape transect for each site. Within each "L" transect, one 200 meter transect line was selected parallel to the predominant snowdrift pattern, and the other 200 meter transect line was made perpendicular to this predominant snowdrift pattern. For most site locations, the parallel transect line is generally oriented from SW to NE, while the perpendicular transect line is oriented from NW to SE. Snow depth was measured every one meter along the two linear transect lines for each study site, for a total of 400 snow depth measurements at each of the 20 sites. The measured snow depths from all 20 sites ranges from 2 to 59 cm, with the mean snow depth for the 20 study sites varying from 12 to 18 cm (Fig. 3).

4.5. Meteorological data

An autonomous 2.75 m tall micro-meteorological station was erected in Dease Strait from April 25 to June 26, 2014, to measure on-ice air temperature, wind speed and direction, relative humidity, atmospheric pressure, and down-welling and up-welling radiation fluxes at 1-second intervals (Fig. 4). The tower was inoperable from May 1 to May 7 due to technical issues. The on-ice temperature at the micro-meteorological station ranged from −18 °C to +4 °C during May 2014 and ranged from −11 °C to +7 °C during June 2014. Hereafter, on-ice air temperature refers to the 2 m air temperature that was measured at the micro-meteorological station.

Precipitation data was acquired from the Environment Canada Cambridge Bay weather station (69.108N, 105.338W), which is terrestrially located between 10 and 40 km from our various study sites. <1 cm snowfall was recorded in early April and over 20 cm of meteoric snow was recorded in May (Fig. 4). However, the airport weather station is more sheltered than the open sea ice area. Strong winds occurred on the ice for much of May and early June, and this likely caused some snow redistribution over the study sites.

4.6. Incidence angle correction

In the acquired SIR format ASCAT backscatter data, we observed a five-day cyclical pattern that does not reflect physical or dielectric changes in surface conditions (Fig. 5a). We attribute the cyclical behavior to an improper application of incidence angle dependency (slope) for FYI during incidence angle normalization. During cold winter conditions (e.g. before 2014-05-11), the SIR incidence angle slope follows a distinct five-day cycle (Fig. 5b), although a consistent incidence angle dependency is expected (Makynen et al., 2002).

To reduce the effects of the varying incidence angle slope, we first reverse the daily incidence angle normalization as a function of the mean daily incidence angle, which also varies on a five-day cycle:

$$a' = a - (j - 40)b \tag{1}$$

where, a is the mean backscatter (normalized to 40°); j is the mean daily incidence angle; and b is the mean daily incidence angle slope; a, j and b are provided in the SIR product.

We then normalize the backscatter to 49° incidence angle by applying a consistent incidence angle slope of 0.29/°:

$$\sigma^0_{adj} = a' + (j - 49) \cdot 0.29 \tag{2}$$

A slope of 0.29/° is used because it is midway between reported values for smooth FYI during dry winter and wet melt periods (Makynen et al., 2002), which are both relevant to our study. Applying this value also minimizes the pre-melt backscatter standard deviation,

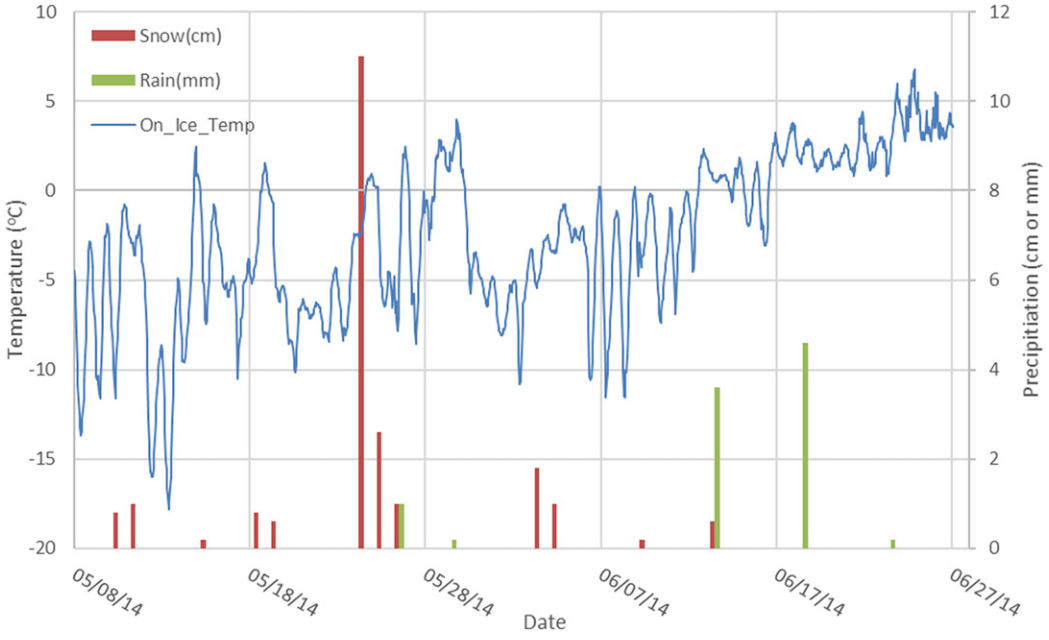

Fig. 4. Time series of hourly measured air temperature at the on-ice meteorological station and precipitation on land at the Cambridge Bay, Nunavut weather station.

supporting its use. We use an incidence angle of 49° for normalization because it represents the mean incidence angle for the study area and period, and thus minimizes the adjustment needed during normalization.

Application of Eqs. (1) and (2) considerably reduces the five-day cycling during the winter season (Fig. 5c).

4.7. Melt-onset (MO) detection

Pre-melt conditions on snow covered FYI as detected by ASCAT can be described as low and stable σ° values that are typical of winter sea ice scattering (Livingstone et al., 1987; Barber et al., 1994). ASCAT melt onset (MO) over smooth FYI is denoted by the first sharp upturn from the stable winter period. This upturn is attributed to increased volume scattering due an increase in brine volume associated with large snow grains in the basal layer (Barber et al., 1995). To avoid false alarms in the detection of MO, we set a minimum daily mean air temperature threshold at −5 °C, as snow is unlikely to experience melting below that threshold (Mahmud et al., 2016). To identify the transition from winter to MO, we use the change threshold ($\Delta\sigma^\circ_{TR}$) of 2.8 dB from Mahmud et al. (2016), which is calculated for C-band backscatter of snow covered FYI in the Canadian Arctic from 1997 to 2014. The $\Delta\sigma^\circ_{TR}$ value of 2.8 dB is obtained for HH-polarization; however, VV-polarization is expected to behave similarly for smooth FYI (e.g. Nghiem et al., 1995; Geldsetzer and Yackel, 2009). We identify the MO date as one day prior to the day $\Delta\sigma^\circ$ reaches and/or crosses 2.8 dB for the first time:

$$\Delta\sigma^\circ = \sigma^\circ - \sigma^\circ_{Mean} \quad (3)$$

If $\Delta\sigma^\circ \geq \Delta\sigma^\circ_{TR}$, MO detected

If $\Delta\sigma^\circ < \Delta\sigma^\circ_{TR}$, Pre-MO detectedwhere σ° is the backscatter value, σ°_{Mean} is the mean winter backscatter based on the April and early May σ° when air temperatures are below −5 °C.

4.8. Time-series MODIS band 1 WSA

4.8.1. Pond-onset (PO) detection

The shortwave albedo of snow covered FYI is generally high and stable (>0.8 but <0.95) throughout winter and early melt, and decreases only slightly during the melt onset transition; however, a rapid decrease in albedo occurs as soon as ponding begins (PO). Given this sensitivity, we use albedo from the daily MODIS product to identify PO. Typically, a rapid, large decrease in albedo occurs as melt ponds continue to form in the days to weeks following PO; albedo decreases to as low as 0.2 (Polashenski et al., 2012). There may be intermittent increases in albedo during this period as snow storms frequent the region and deposit fresh snow. To identify PO from MODIS albedo, we calculate a threshold albedo using a linear function associating sea ice albedo and pond fraction:

$$A_{TR} = A_0 - A_l * P \quad (4)$$

where, A_0 and A_l are coefficients, and P is the pond fraction. Morassutti and LeDrew (1995) summarize several coefficients for A_0 and A_l; we take an average of their values, resulting in $A_0 = 0.62$ and $A_l = 0.45$. We use a 10% pond fraction to represent PO, thus $P = 0.1$. The resulting threshold $A_{TR} = 0.58$.

The albedo threshold for PO is used as a filter for the time series MODIS albedo data, and a specific PO date is obtained for each pixel within our study area. This PO date is then used as input to the degree-day model in order to estimate a pixel-based snow thickness distribution.

4.9. Snow melt model

A simple degree-day model at an hourly time step is use to estimate the snow thickness in late winter immediately prior to MO (Kane et al., 1997):

$$M = C_0\,(Ta - T_0)/s \quad (5)$$

where M is snowmelt (mm/h); C_0 is a melt coefficient (mm/d °C) to be calibrated; Ta is hourly air temperature; T_0 is the threshold air temperature coefficient, which is set to −0.44 °C after Mahmud et al. (2016); and s is the number of time steps per day, 24.

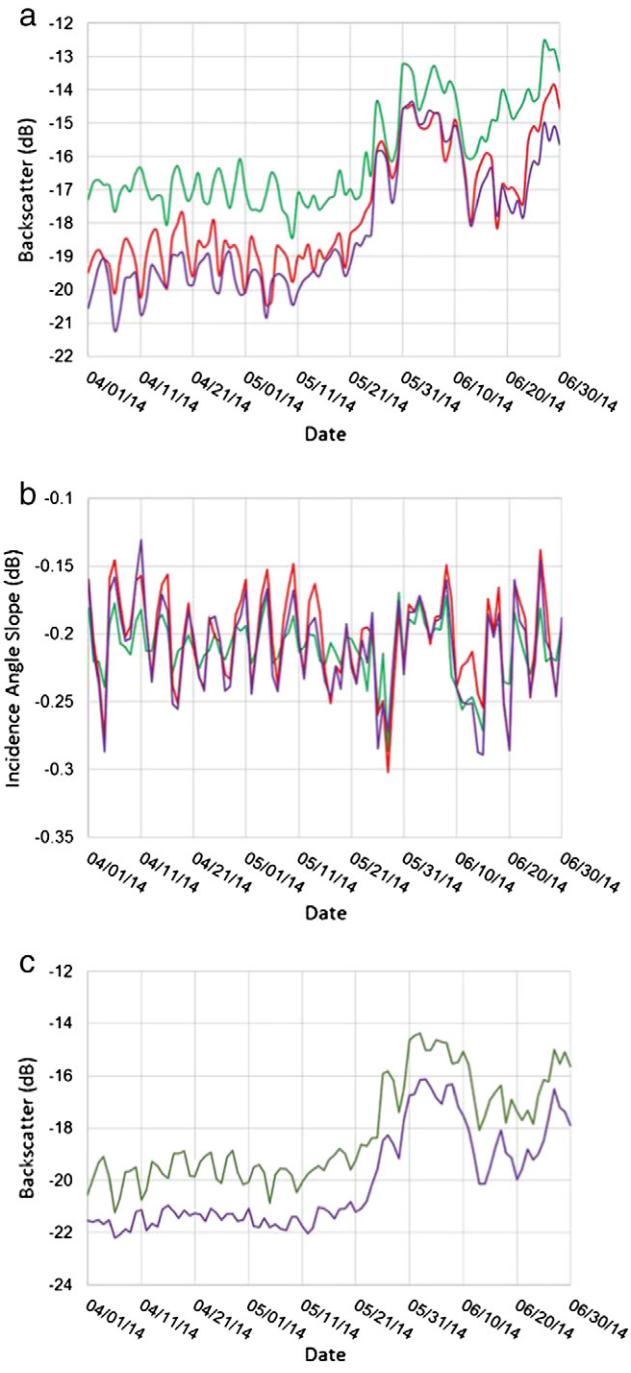

Fig. 5. a. Mean daily backscatter reported by SIR product, normalized to 40° incidence angle, for sea ice in Dease Strait, Nunavut, for three test sites: Site A (green), Site B (red) and Site C (purple). b. Mean daily incidence angle slope used to adjust ASCAT scatterometer measurements from sea ice in Dease Strait, Nunavut, for three test sites: Site A (green), Site B (red) and Site C (purple). c.Mean daily backscatter from sea ice in Dease Strait, Nunavut, for Test Site C. The green line is the SIR backscatter normalized to 40°. The purple line is the backscatter normalized to 49° following removal of the original incidence angle slope, based on Eqs. (1) and (2).

C_0, the melt coefficient is calibrated using in-situ PO observation and snow thickness measurements. PO was visually observed in situ on June 17, 2014, at 69.030, 105.336 (Aura Diaz personal communication). Three surrounding study sites (B2, B6 and C3) are located in close proximity to the PO observation site (~2 km away). The mean snow thickness of the three sites is 15.6 ± 8.2 cm; this mean snow thickness value is used to represent the snow thickness of the PO observation site. C_0 is thus the value required to melt 15.6 cm of snow between MO and PO.

The melt model is applied to each pixel in the MODIS data once a pixel reaches PO. For each pixel, the hourly air temperature between MO and PO is used to run the model, in order to estimate the thickness of snow that needs to be melted to arrive at PO. This provides a pixel-based estimate of the snow thickness within the study area. Snow thickness data from the remaining 17 study sites are used to assess the performance of the model, and produce an accuracy assessment.

5. Results and discussion

5.1. ASCAT time series

The time-series of daily mean air temperature and ASCAT σ° from three smooth FYI sites with different mean snow thickness are illustrated (Fig. 6). The vertical grey dashed line on the figure depicts the ASCAT-detected date of MO (May 24), consistent with a sharp rise in σ° from its winter mean (Eq. (3)). MO occurs on the same day throughout the study area. The pre-melt period (*winter*) from April 1 to May 23, exhibits low, relatively stable backscatter at ~ −21 dB ± 1.5 dB, when air and snow temperatures are consistently below −5 °C. The stable low *winter* σ° level for FYI is attributable to low surface scattering from smooth snow-ice interface and microwave absorption by the brine-wetted basal snow layer (Barber and Nghiem, 1999; Howell et al., 2006). ASCAT σ° from FYI exhibits many small variations during *winter*. These variations in σ° are likely in response to air temperature

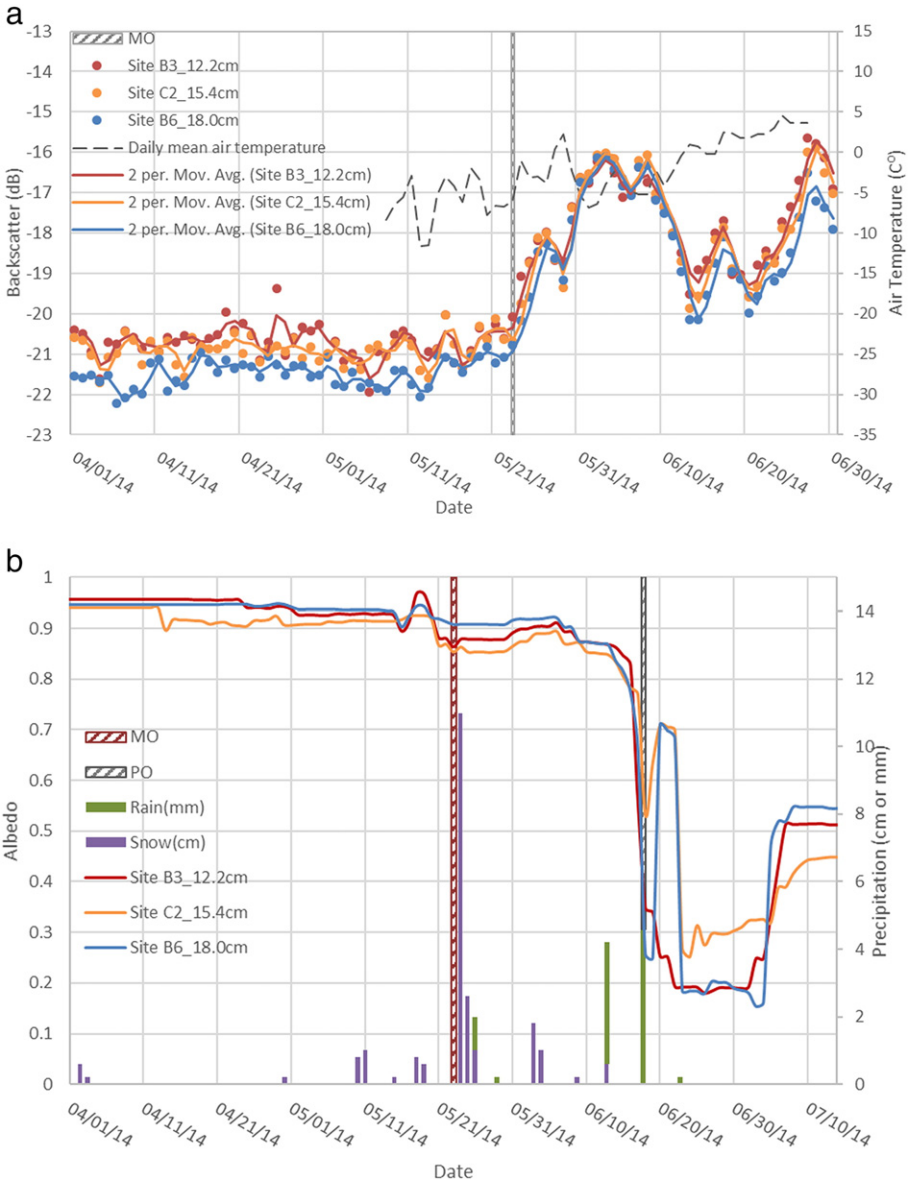

Fig. 6. a. Time series of normalized daily ASCAT backscatter are plotted for site B2, B6 and C3 in conjunction with daily air temperature data. The mean snow thickness of each sample site is shown in the legend. MO for these three sample sites is marked by the grey dashed bar. The curves are 2-point moving averages and are for visualization only. b. Time series of daily MODIS albedo for site B2, B6 and C3 in conjunction with daily precipitation data acquired from the Cambridge Bay Airport weather station. ASCAT detected MO is marked by the red dashed bar. PO for these three sample sites is marked by the grey dashed bar.

changes, with differences as a function of snow thickness. The variation of σ° is a function of differences in volume scattering from geophysical changes to the brine-wetted snow at the base of snowpack, and upper layer (few mm) of sea ice, due to temperature-brine influences (Barber and Nghiem, 1999). Since thick snow acts to dampen temperature variations at base of the snowpack relative to thinner snow, backscatter from the thinnest snow site in Figs. 6a and b (red line) fluctuates the most during *winter*.

The post-MO period exhibits highly variable backscatter, consistent with increasing snow surface wetness, increasing brine volume in the basal snow layers, transition from pendular to funicular regimes, pond onset and finally pond drainage (Colbeck, 1982; Barber et al., 1995; Barber and Yackel, 1999; Yackel and Barber, 2000; Yackel et al., 2007; Scharien et al., 2014). The identification of PO in single polarization SAR imagery has inherent ambiguity, given the competing effects of pond fraction, pond wind roughening, and ice roughness. Therefore, optical (MODIS) data are used to detect PO.

5.2. MODIS albedo time series

Time-series albedo from daily MODIS in conjunction with precipitation data is plotted for the same three smooth FYI sites, plus a two week extension (until July 14) to show albedo values during the *advanced melt* stage (Fig. 6b). The vertical grey dashed line in the figure depicts the MODIS-detected date of PO for these three sites, which happen to be on the same day (June 17th), consistent with a sharp drop in albedo from ~0.80 to ~0.50 within one day. During the cold period in April and early May before MO, MODIS albedo is consistently above 0.9 for all the sites, and albedo at all three sites are similar because of the snow cover. The variations during the pre-melt period are likely attributable to periodic snowfall, which acts to increase the albedo slightly.

At ASCAT detected MO (May 24), the albedo experiences a slight decrease from ~0.93 to ~0.87, which can be associated with coarsening of snow grains and small quantities of liquid water beginning to appear within the snowpack during periods of increased shortwave flux during the day (Grenfell and Perovich, 2004). However, the albedo does not continue to drop after ASCAT detected MO due to several precipitation events, in the form of snow, in the subsequent three weeks following MO. The temperature remains near the freezing point, and together with the intermittent snowfall, the albedo increases slightly and remains mostly steady in the following two weeks. On June 13, with air temperature exceeding 0 °C, and an associated rain event, the albedo decreases rapidly. On June 17, the albedo for all three sites decreases below the threshold A_{TR} of 0.58, marking PO. At PO, albedo reflects a mixed-pixel signature of melt ponds and snow/ice patches. The reason for the rebound in albedo after PO, for Sites B6 and C2, is uncertain. It may be that meteoric snow fell on the remaining snow/ice patches during what was a rain event on land near Cambridge Bay, increasing the mixed-pixel albedo; while Site B3, the thinnest site, may already have had extensive ponding, thus not allowing snow to accumulate. After June 21, all three sites exhibit albedo values consistent with extensive melt ponding. The subsequent increase in albedo in early July is likely due to pond drainage thereby exposing the remaining drained ice patches.

5.3. Degree-day snowmelt model

The melt coefficient C_0, used in the degree-day snowmelt model, is calibrated to a value of 9.7 mm/d °C. This value is larger than most melt coefficients reported for snow on glacier or snow on lake ice (e.g. Kane et al., 1997; Hock, 2003; Hughes and Braithwaite, 2008). It is within the range of melt coefficients for snow on Himalayan glaciers; however, it is more similar to coefficients for snow on glacier ice (Hock, 2003). The larger value is most likely related to the effect of the brine-wetted basal layer of the snow cover towards increasing the thermal heat capacity of the volume.

The accumulated melted snow thickness using the calibrated degree-day snowmelt model (at hourly time steps) from MO (May 24) through advanced melt (end of June) is illustrated in Fig. 7. The vertical grey dashed line depicts the PO date (June 17) for the three sample sites discussed previously (sites B3, B6, and C2). At MO, the air temperature only exceeds T_0 for 18 h and only reaches 0.7 °C, thus modeled melt is limited to <1 cm. A subsequent brief melt period occurs on May 26. This is followed by a longer melt period between May 28 and May 30, which melts ~7 cm of snow. Therefore, by May 30, melt ponds may have formed in shallow areas of the snow cover. However, the air temperature drops below T_0 for the next week, and then only briefly exceeds T_0 on several days until June 12, resulting in <0.3 cm of snow to melt during this period. With diurnal fluctuations above and below 0 °C, melting again progresses after June 12, and snowmelt proceeds slowly (~1 cm/day). By June 17, 14.6 cm of snow has melted; this is the estimated pre-MO snow thickness for sample sites B3, B6, and C2. Air temperature thereafter remains above 0 °C, where the melt rate increases to ~3.5 cm/day and we observe a nearly linear increase in the accumulated melted snow thickness beyond June 17.

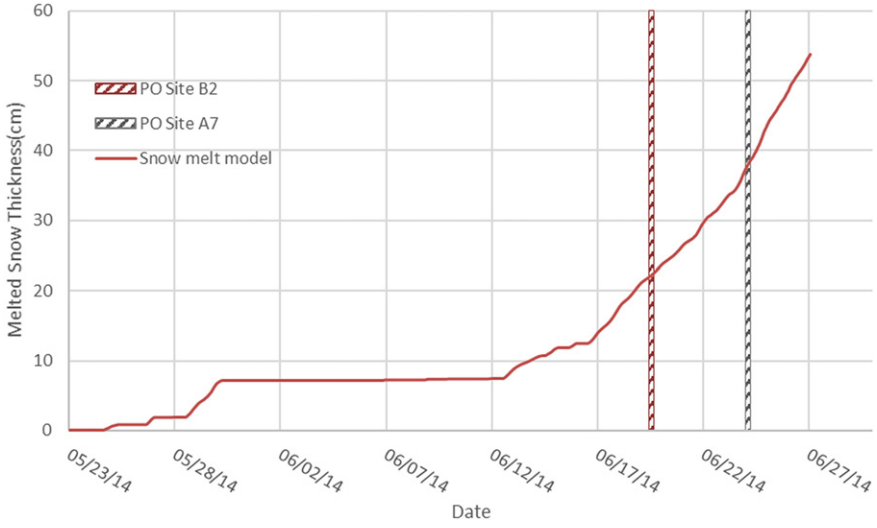

Fig. 7. Degree-day snowmelt model results based on on-ice hourly air temperature and a melt coefficient of 9.7 mm/d °C. The model represents the snow melting process of all MODIS pixels. The red dashed vertical bar marks the PO date of Site B2 and the grey dashed vertical bar marks the PO date of Site A7, which are also the date that the snowmelt model stops running (end of snowmelt duration) for those sites.

Using the study-area-wide MO date from ASCAT, and PO dates estimated from the time-series albedo for each of the MODIS pixels, we run the degree-day model on a pixel by pixel basis for a ~25 × 50 km area in Dease Strait, thereby covering all 20 of our study sites (Fig. 8). Most of the thin snow cover is found adjacent to the south shore (dark blue pixels on the map); whereas, the snow near the north shore is thicker (>21.4 cm). We speculate that the primary physical mechanism responsible for this pattern is that during late fall/early winter (October–December 2013), FYI formed and consolidated earlier within the bay and inlet along the north shore near Cambridge (Bay). Because ice forms earlier within calm bay waters compared to the Strait waters to the south, landfast ice would have formed earlier along the north shore of Dease Strait. According to ice charts from Canadian Ice Service, the north shore of Dease Strait formed new ice on October 26, 2013, while the south shore of Dease Strait was still open water. Thus, more fall snow is likely to have accumulated on the early-consolidated ice along the north shore of Dease Strait.

Medium mean snow thickness (~14–21 cm) is estimated for most of Dease Strait, which generally agrees with our measured data. There are some thick snow areas in the middle of Dease Strait, and most of these are associated with rougher FYI areas. Because rough FYI tends to catch more snow than the smoother FYI, snow cover is generally thicker on rough FYI compared to smooth FYI (Iacozza and Barber, 1999, 2010).

The resulting snow thickness estimations agree reasonably well with measured snow thickness for most of the test sites, as is indicted by a mean bias error (MBE) of 0.3 cm and a RMSE of 4.0 cm (Table 2). However, among the 17 test sites, the modeled results of site A3, A7 and C1 show relatively large bias. The accuracy assessment shows large positive bias for site A3 and A7, which could be due to the ridges crossing the pixels at these two sites. Ridges have higher albedo than

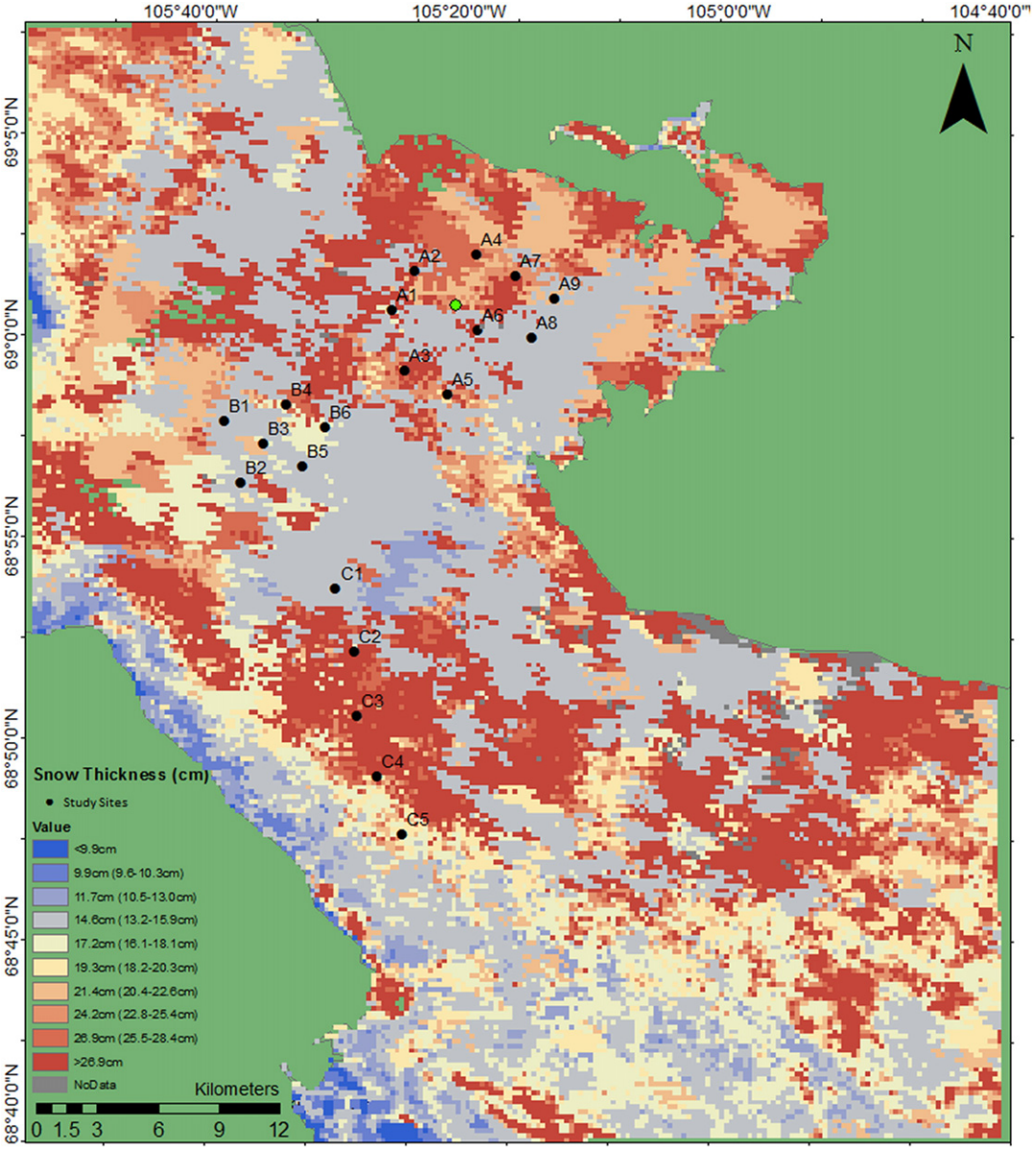

Fig. 8. Estimated snow thickness spatial distribution in Dease Strait, Nunavut southwest of Cambridge Bay for late winter 2014. Pixels correspond to MODIS data. Green areas are land that has been masked out; grey pixels are NoData values associated with MODIS data. The green dot in the cluster of in situ validation points (A 1–9) is the model calibration location. The displayed depth categories are based on snowmelt durations. The snow thickness ranges shown in the legend indicate the minimum and maximum snow thickness estimate for the 24-hour period. The snowmelt model provides hourly data, whereas the MODIS data are daily; this necessitates a snow thickness range instead of a single value.

smooth FYI, thus delaying the detection of PO and overestimating the snowmelt.

5.4. Error analysis and discussion

Generally, errors could occur at several stages throughout a study. For this study, we place the possible error sources into three categories including field data errors, satellite data errors and model calibration errors.

For field data, errors could occur during manual snow thickness measurements and logging. Any errors of the measurement tool (i.e. a metal ruler) and misreading of the measurement values could lead to an accumulating error for the snow thickness of a site. Also, logging error could be an error source of random errors, which is more likely to happen during inclement weather (i.e. cold and windy).

For satellite data, errors could occur during threshold selection (i.e. albedo threshold for PO) and during data preparation (i.e. data inversion). As discussed earlier, we adopted a linear regression function as well as several parameters from previous studies to calculate the threshold of albedo at PO. However, we cannot guarantee that the calculated threshold does represent the true PO albedo for the entire area due to lacking of field measurement. The PO detection result based on the threshold is used as an input of the snowmelt model, and therefore, any error in the threshold could affect results stemming from the modelling. On the other hand, since the daily MODIS albedo data are based on the inversion of available cloud-free images within a 16-day window, the modeled daily albedo may contain possible errors/bias.

Finally, for model calibration, errors may occur due to the mismatch between the timing of field measurements (used in calibration) and the timing of satellite detected MO. The field measurements for snow thickness were conducted during the third week of April (19th, 20th, and 22nd), 2014, and these measurements were then used as the snow thickness at MO, which is detected to occur on May 23rd for model calibration. There is a time mismatch of about one month between the actual MO and when the field data were collected, and therefore, any significant precipitation between these dates could lead to errors/bias in the model calibration.

For the Degree-day snowmelt model, one limitation is that no precipitation after MO is considered as input to the model, which may bias the estimated late winter snow thickness. Any precipitation after MO could change the snow thermal-physical properties and the current snow thickness rapidly, by adding fresh snow or water into the snow cover. Moreover, the melt coefficient may exhibit considerable spatial and temporal variability, and this may vary with weather and surface type (Hock, 2003). For snow covered FYI, due to the relatively lower small-scale horizontal variability compared other terrain (i.e. mountain area), the melt coefficient calibrated from a small amount of field measurements can generally be assumed representative on the regional scale.

Therefore, future studies should focus on adding precipitation after MO as a model input and testing this methodology over different FYI regions for a similar time period in a year and even adjust the melt coefficient to adapt to other ice types in Canadian Arctic Archipelago. Once this methodology has been tested to show robustness, it could be useful for long-term snow/sea ice monitoring, and it can also provide up-to-date snow information for climate models.

The overall performance of this methodology provides reasonable results for regional snow thickness estimation. Moreover, the methodology shows promise for upscaling without large data requirements. However, some limitations of the degree-day snowmelt model are that the melt coefficient may exhibit considerable spatial and temporal variability because it is highly dependent on the local energy balance, weather and surface type (Hock, 2003). For homogeneous snow covered FYI, due to the relatively lower small-scale variability compared with other terrain (i.e. mountainous areas), the melt coefficient calibrated from a small amount of field measurements can be assumed representative on a regional scale. Another limitation is that any precipitation after MO is not considered in the model. Precipitation after MO could change the snow thermal-physical properties and the current snow thickness rapidly, by adding fresh snow or water into the snow cover; additional snow accumulation would likely result in an overestimation of pre-MO snow thickness, whereas rain would likely cause an underestimation of pre-MO snow thickness. Future studies could focus on adding precipitation after MO as a model input and testing the robustness of the melt coefficient used in this study in other FYI regions.

Table 2
Accuracy assessment of degree-day snowmelt model against 17 in situ measurements.

Field site	Field measured snow thickness (cm)	Modeled snow thickness (cm)	Snow melt duration (day)	Bias
A1	16.1 ± 10.9	14.6 ± 0.8	24.5	−1.5
A3	12.3 ± 5.4	19.3 ± 0.6	26.5	7.0
A5	13.1 ± 8.0	17.2 ± 0.6	25.5	4.1
A7	12.5 ± 4.8	21.4 ± 0.6	27.5	8.9
A8	13.9 ± 6.2	11.7 ± 0.7	23.5	−2.2
A9	14.7 ± 5.6	11.7 ± 0.7	23.5	−3.0
B1	13.6 ± 4.9	11.7 ± 0.7	23.5	−1.9
B2	14.8 ± 8.3	11.7 ± 0.7	23.5	−3.1
B3	12.2 ± 4.6	14.6 ± 0.8	24.5	2.4
B4	14.2 ± 5.9	14.6 ± 0.8	24.5	0.4
B5	15.3 ± 6.5	11.7 ± 0.7	23.5	−3.6
B6	18 ± 7.4	14.6 ± 0.8	24.5	−3.4
C1	17.8 ± 8.2	11.7 ± 0.7	23.5	−6.1
C2	15.4 ± 6.1	14.6 ± 0.8	24.5	−0.8
C3	14.1 ± 8.0	14.6 ± 0.8	23.5	0.5
C4	14.5 ± 8.1	19.3 ± 0.6	26.5	4.8
C5	12.6 ± 7.3	14.6 ± 0.8	24.5	2.0
Mean	14.4	14.7	24.6 ± 1.2	/
RMSE	/	4.0 cm (27.1%)	/	/
Mean bias	/	/	/	0.3 cm (1.8%)

6. Summary

This study investigates late winter snow thickness on first-year sea ice in Dease Strait near Cambridge Bay, NU based on the duration of snowmelt and in situ acquired snow thickness data. Daily spaceborne C-band microwave scatterometer backscatter and optical MODIS albedo are used to estimate the duration of snowmelt on a per pixel basis. Scatterometer noise cycling removal and incidence angle normalization is applied to the daily all-passes ASCAT data used to identify snow MO timing for the study area. A MO date of May 24 is identified by the first sharp increase in σ° in the wintertime series exceeding the change threshold; a single MO date is found for the entire study area. PO is detected using time-series MODIS albedo assuming at least 10% pond fraction within each pixel, and coincides with a rapid, large decrease in albedo for each pixel. A simple degree-day snowmelt model is applied based on air temperature and tested using in situ acquired snow thickness and snowmelt observations on FYI collected in Dease Strait, NU between April and June 2014. The model accuracy assessment yields a mean bias error of 0.3 cm and a RMSE of 4.0 cm. We recommend attempting to repeat this experiment in future years to compare to the melt coefficient derived here.

Acknowledgment

The authors wish to thank participants of the ICE-CAMPS 2014 experiment (C.J. Mundy, P.I.) In particular, we wish to thank M. Mahmud, University of Calgary, for data collection efforts. We also wish to thank NSERC for a Discovery Grant to J. Yackel, the Polar Continental Shelf Program (PCSP) – NRCan (Project# 62214); ArcticNet - an NSERC Centers of Excellence; Arctic Research Foundation and the Canadian High Arctic Research Station (CHARS) for their financial and logistical support.

References

Arendt, A., Sharp, M., 1999. Energy balance measurements on a Canadian high arctic glacier and their implications for mass balance modelling. Proc. IUGG Symp., Birmingham 1999: Interactions Between the Cryosphere, Climate and Greenhouse Gases. International Union of Geodesy and Geophysics, Birmingham, United Kingdom, pp. 165–172.

Arnold, K.C., Mackay, D.K., 1964. Different methods of calculating mean daily temperatures, their effects on degree-day totals in the high arctic and their significance to glaciology. Geogr. Bull. 21, 123–129.

Barber, D.G., LeDrew, E.F., 1994. On the links between microwave and solar wavelength interactions with snow-covered first-year sea ice. Arctic 47 (3), 298–309.

Barber, D.G., Nghiem, S.V., 1999. The role of snow on thermal dependence of microwave backscatter over sea ice. J. Geophys. Res. 104 (C11), 25789–25803.

Barber, D.G., Thomas, A., 1998. The influence of cloud cover on the radiation budget, physical properties, and microwave scattering coefficient (σ°) of first-year and multiyear sea ice. IEEE Trans. Geosci. Remote Sens. 36 (1), 38–50.

Barber, D.G., Yackel, J.J., 1999. The physical, radiative and microwave scattering characteristics of melt ponds on Arctic landfast sea ice. Int. J. Remote Sens. 20 (10), 2069–2090.

Barber, D.G., Papakyriakou, T.N., LeDrew, E.F., 1994. On the relationship between energy fluxes, dielectric properties, and microwave scattering over snow covered first-year sea ice during the spring transition period. J. Geophys. Res. 99 (C11), 22401–22411.

Barber, D.G., Reddan, S.P., LeDrew, E.F., 1995. Statistical characterization of the geophysical and electrical properties of snow on landfast first-year sea ice. J. Geophys. Res. 100 (C2), 2673–2686.

Barber, D.G., Fung, A.K., Grenfell, T.C., Nghiem, S.V., Onstott, R.G., Lytle, V.L., Perovich, D.K., Gow, A.J., 1998. The role of snow on microwave emission and scattering over first-year sea ice. IEEE Trans. Geosci. Remote Sens. 36 (5), 1750–1763.

Braithwaite, R.J., Konzelmann, T., Marty, C., Olesen, O.B., 1998. Errors in daily ablation measurements in northern Greenland, 1993–94, and their implications for glacier climate studies. J. Glaciol. 44 (148), 583–588.

Brandt, R.E., Warren, S.G., Worby, A.P., Grenfell, T.C., 2005. Surface albedo of the Antarctic sea ice zone. J. Clim. 18 (17), 3606–3622.

Brown, R.D., Cote, P., 1992. Interannual variability of landfast ice thickness in the Canadian High Arctic, 1950–89. Arctic 273–284.

Clyde, G.D., 1931. Snow-melting characteristics. Utah Agric. Exp. Station. Bull. 231, 1–23.

Colbeck, S.C., 1979. Water flow through heterogeneous snow. Cold Reg. Sci. Technol. 1 (1), 37–45.

Colbeck, S.C., 1982. An overview of seasonal snow metamorphism. Rev. Geophys. 20 (1), 45–61.

Colbeck, S.C., 1983. Theory of metamorphism of dry snow. J. Geophys. Res. 88 (C9), 5475–5482.

Colbeck, S.C., Thorndike, A.S., Whillans, I.M., Hodge, S.M., Ackley, S.F., Ashton, G.D., 1975. Snow and ice. Rev. Geophys. 13 (3), 435–441.

Collins, E.H., 1934. Relationship of degree-days above freezing to runoff. EOS Trans. Am. Geophys. Union 15 (2), 624–629.

Drinkwater, M.R., Crocker, G.B., 1988. Modelling changes in the dielectric and scattering properties of young snow-covered sea ice at GHz frequencies. J. Glaciol. 34 (118), 274–282.

Early, D.S., Long, D.G., 2001. Image reconstruction and enhanced resolution imaging from irregular samples. IEEE Trans. Geosci. Remote Sens. 39 (2), 291–302.

Eicken, H.A.J.O., Lemke, P., 2001. The response of polar sea ice to climate variability and change. In: Lozán, et al. (Eds.), Climate of the 21st Century, Changes and Risks. GEO, Hamburg/Germany, pp. 206–211.

Eicken, H., Krouse, H.R., Kadko, D., Perovich, D.K., 2002. Tracer studies of pathways and rates of meltwater transport through Arctic summer sea ice. J. Geophys. Res. 107 (C10):8046. http://dx.doi.org/10.1029/2000JC000583.

Eicken, H., Grenfell, T.C., Perovich, D.K., Richter-Menge, J.A., Frey, K., 2004. Hydraulic controls of summer Arctic pack ice albedo. J. Geophys. Res. 109, C08007. http://dx.doi.org/10.1029/2003JC001989.

Figa-Saldaña, J., Wilson, J.J., Attema, E., Gelsthorpe, R., Drinkwater, M.R., Stoffelen, A., 2002. The advanced scatterometer (ASCAT) on the meteorological operational (MetOp) platform: a follow on for European wind scatterometers. Can. J. Remote. Sens. 28 (3), 404–412.

Gao, F., Schaaf, C.B., Strahler, A.H., Lucht, W., 2001. Using a multikernel least-variance approach to retrieve and evaluate albedo from limited bidirectional measurements. Remote Sens. Environ. 76 (1), 57–66.

Geldsetzer, T., Yackel, J.J., 2009. Sea ice type and open water discrimination using dual co-polarized C-band SAR. Can. J. Remote. Sens. 35 (13), 73–84.

Golden, K.M., Ackley, S.F., Lytle, V.I., 1998. The percolation phase transition in sea ice. Science 282 (5397), 2238–2241.

Grenfell, T.C., Perovich, D.K., 2004. Seasonal and spatial evolution of albedo in a snow-ice-land-ocean environment. J. Geophys. Res. 109 (C1), 5–10.

Grenfell, T.C., Barber, D.G., Fung, A.K., Gow, A.J., Jezek, K.C., Knapp, E.J., Tanis, F., 1998. Evolution of electromagnetic signatures of sea ice from initial formation to the establishment of thick first-year ice. IEEE Trans. Geosci. Remote Sens. 36 (5), 1642–1654.

Hall, D.K., Kelly, R.E., Foster, J.L., Chang, A.T., 2005. Estimation of snow extent and snow properties. Encycl. Hydrol. Sci. 811–829.

Hanesiak, J.M., Barber, D.G., De Abreu, R.A., Yackel, J.J., 2001. Local and regional albedo observations of arctic first-year sea ice during melt ponding. J. Geophys. Res. 106 (C1), 1005–1016.

Hock, R., 2003. Temperature index melt modelling in mountain areas. J. Hydrol. 282 (1), 104–115.

Hoinkes, H., Steinacker, R., 1975. Zur parametrisierung der beziehung klima-gletscher. Riv. Ital. Geofis. Sci. Affini 1, 97–104.

Holt, B., Digby, S., 1985. Processes and imagery of first-year fast sea ice during the melt season. J. Geophys. Res. 90 (C3), 5045–5062.

Howell, S.E., Tivy, A., Yackel, J.J., Scharien, R.K., 2006. Application of a SeaWinds/QuikSCAT sea ice melt algorithm for assessing melt dynamics in the Canadian Arctic Archipelago. J. Geophys. Res. Oceans 111, C07025. http://dx.doi.org/10.1029/2005JC003193.

Hughes, P.D., Braithwaite, R.J., 2008. Application of a degree-day model to reconstruct Pleistocene glacial climates. Quat. Res. 69, 110–116.

Iacozza, J., Barber, D.G., 1999. An examination of the distribution of snow on sea-ice. Atmosphere-Ocean 37 (1), 21–51.

Iacozza, J., Barber, D.G., 2001. Ablation patterns of snow cover over smooth first-year sea ice in the Canadian Arctic. Hydrol. Process. 15 (18), 3559–3569.

Iacozza, J., Barber, D.G., 2010. An examination of snow redistribution over smooth landfast sea ice. Hydrol. Process. 24 (7), 850–865.

IPCC, 2013. In: Stocker, T.F., Qin, D., Plattner, G.-K., Tignor, M., Allen, S.K., Boschung, J., Nauels, A., Xia, Y., Bex, V., Midgley, P.M. (Eds.), Climate Change 2013: The Physical Science Basis. Contribution of Working Group I to the Fifth Assessment Report of the Intergovernmental Panel on Climate Change. Cambridge University Press, Cambridge, United Kingdom and New York, NY, USA 1535 pp.

Irvine, W.M., Pollack, J.B., 1968. Infrared optical properties of water and ice spheres. Icarus 8 (1–3), 324–360.

Jin, Y., Schaaf, C.B., Gao, F., Li, X., Strahler, A.H., Lucht, W., Liang, S., 2003a. Consistency of MODIS surface bidirectional reflectance distribution function and albedo retrievals: 1. Algorithm performance. J. Geophys. Res. Atmos. 108 (D5).

Jin, Y., Schaaf, C.B., Woodcock, C.E., Gao, F., Li, X., Strahler, A.H., Liang, S., 2003b. Consistency of MODIS surface bidirectional reflectance distribution function and albedo retrievals: 2. Validation. J. Geophys. Res. Atmos. 108 (D5).

Kane, D.L., Gieck, R.E., Hinzman, L.D., 1997. Snowmelt modeling at small Alaskan Arctic watershed. J. Hydrol. Eng. 2 (4), 204–210.

Kurtz, N.T., Farrell, S.L., Studinger, M., Galin, N., Harbeck, J.P., Lindsay, R., Onana, V.D., Panzer, B., Sonntag, J.G., 2013. Sea ice thickness, freeboard, and snow depth products from Operation IceBridge airborne data. Cryosphere 7:1035–1056. http://dx.doi.org/10.5194/tc-7-1035-2013.

Kustas, W.P., Rango, A., Uijlenhoet, R., 1994. A simple energy budget algorithm for the snowmelt runoff model. Water Resour. Res. 30 (5), 1515–1527.

Kuusisto, E., 1984. Snow accumulation and snowmelt in Finland. Nord. Hydrol. 11, 235–242.

Kwok, R., Rothrock, D.A., 2009. Decline in Arctic sea ice thickness from submarine and ICESat records: 1958–2008. Geophys. Res. Lett. 36 (15), 1–5.

Lindsay, R., Schweiger, A., 2015. Arctic sea ice thickness loss determined using subsurface, aircraft, and satellite observations. Cryosphere 9:269–283. http://dx.doi.org/10.5194/tc-9-269-2015.

Lindsley, R.D., Long, D.G., 2010. Adapting the SIR algorithm to ASCAT. Geoscience and Remote Sensing Symposium (IGARSS), 2010 IEEE International:pp. 3402–3405 http://dx.doi.org/10.1109/IGARSS.2010.5650207.

Liu, J., Schaaf, C., Strahler, A., Jiao, Z., Shuai, Y., Zhang, Q., Dutton, E.G., 2009. Validation of Moderate Resolution Imaging Spectroradiometer (MODIS) albedo retrieval algorithm: dependence of albedo on solar zenith angle. J. Geophys. Res. Atmos. 114 (D1).

Livingstone, C.E., Drinkwater, M.R., 1991. Springtime C-band SAR backscatter signatures of Labrador Sea marginal ice: measurements versus modeling predictions. IEEE Trans. Geosci. Remote Sens. 29 (1), 29–41.

Livingstone, C.E., Singh, K.P., Gray, A.L., 1987. Seasonal and regional variations of active/passive microwave signatures of sea ice. IEEE Trans. Geosci. Remote Sens. 2, 159–173.

Long, D.G., Hardin, P.J., Whiting, P.T., 1993. Resolution enhancement of spaceborne scatterometer data. IEEE Trans. Geosci. Remote Sens. 31 (3), 700–715.

Lucht, W., Schaaf, C.B., Strahler, A.H., 2000. An algorithm for the retrieval of albedo from space using semiempirical BRDF models. IEEE Trans. Geosci. Remote Sens. 38 (2), 977–998.

Lytle, V.I., Jezek, K.C., Hosseinmostafa, A.R., Gogineni, S.P., 1993. Laboratory backscatter measurements over urea ice with a snow cover at Ku band. IEEE Trans. Geosci. Remote Sens. 31 (5), 1009–1016.

Maass, N., Kaleschke, L., Tian-Kunze, X., Tonboe, R.T., 2015. Snow thickness retrieval from L-band brightness temperatures: a model comparison. Ann. Glaciol. 56 (69), 9–17.

Mahmud, M.S., Howell, S.E., Geldsetzer, T., Yackel, J., 2016. Detection of melt onset over the northern Canadian Arctic Archipelago sea ice from RADARSAT, 1997–2014. Remote Sens. Environ. 178, 59–69.

Makynen, M.P., Manninen, A.T., Simila, M.H., Karvonen, J.A., Hallikainen, M.T., 2002. Incidence angle dependence of the statistical properties of C-band HH-polarization backscattering signatures of the Baltic Sea ice. IEEE Trans. Geosci. Remote Sens. 40 (12), 2593–2605.

Markus, T., Cavalieri, D.J., Gasiewski, A.J., Klein, M., Maslanik, J.A., Powell, D.C., Stankov, B.B., Stroeve, J.C., Sturm, M., 2006. Microwave signatures of snow on sea ice: observations. IEEE Trans. Geosci. Remote Sens. 44 (11), 3081–3090.

Maslanik, J.A., Fowler, C., Stroeve, J., Drobot, S., Zwally, J., Yi, D., Emery, W., 2007. A younger, thinner Arctic ice cover: increased potential for rapid, extensive sea-ice loss. Geophys. Res. Lett. 34, L24501. http://dx.doi.org/10.1029/2007GL032043.

Maykut, G.A., Untersteiner, N., 1971. Some results from a time-dependent thermodynamic model of sea ice. J. Geophys. Res. 76 (6), 1550–1575.

Morassutti, M.P., LeDrew, E.F., 1995. Melt Pond Dataset for Use in Sea-ice and Climate-related Studies. Earth Observations Laboratory (EOL), Institute for Space and Terrestrial Science (ISTS), and the Department of Geography, University of Waterloo.

Moritz, R.E., Bitz, C.M., Steig, E.J., 2002. Dynamics of recent climate change in the Arctic. Science 297 (5586), 1497–1502.

Mortin, J., Howell, S.E., Wang, L., Derksen, C., Svensson, G., Graversen, R.G., Schrøder, T.M., 2014. Extending the QuikSCAT record of seasonal melt–freeze transitions over Arctic sea ice using ASCAT. Remote Sens. Environ. 141, 214–230.

Nandan, V., Geldsetzer, T., Islam, T., Yackel, J.J., Gill, J.P.S, Fuller, M.C., Gunn, G., Duguay, C., 2016. Ku-, X- and C-band measured and modeled microwave backscatter from a highly saline snow cover on first-year sea ice. Remote Sens. Environ. 187, 62–75.

Nghiem, S.V., Kwok, R., Yueh, S.H., Drinkwater, M.R., 1995. Polarimetric signatures of sea ice 2. Experimental observations. J. Geophys. Res. 100 (C7), 13,681–13,698.

Perovich, D.K., Polashenski, C., 2012. Albedo evolution of seasonal Arctic sea ice. Geophys. Res. Lett. 39, L08501. http://dx.doi.org/10.1029/2012GL051432.

Polashenski, C., Perovich, D., Courville, Z., 2012. The mechanisms of sea ice melt pond formation and evolution. J. Geophys. Res. 117 (C1). http://dx.doi.org/10.1029/2011JC007231.

Post, E., Bhatt, U.S., Bitz, C.M., Brodie, J.F., Fulton, T.L., Hebblewhite, M., Walker, D.A., 2013. Ecological consequences of sea-ice decline. Science 341 (6145), 519–524.

Rango, A., Martinec, J., 1995. Revisiting the degree-day method for snowmelt computations. J. Am. Water Resour. Assoc. 31 (4), 657–669.

Roy, D.P., Lewis, P., Schaaf, C., Devadiga, S., Boschetti, L., 2006. The global impact of clouds on the production of MODIS bidirectional reflectance model-based composites for terrestrial monitoring. IEEE Geosci. Remote Sens. Lett. 3 (4), 452–456.

Salomon, J.G., Schaaf, C.B., Strahler, A.H., Gao, F., Jin, Y., 2006. Validation of the MODIS bidirectional reflectance distribution function and albedo retrievals using combined observations from the aqua and terra platforms. IEEE Trans. Geosci. Remote Sens. 44 (6), 1555–1565.

Schaaf, C.B., Gao, F., Strahler, A.H., Lucht, W., Li, X., Tsang, T., Lewis, P., 2002. First operational BRDF, albedo nadir reflectance products from MODIS. Remote Sens. Environ. 83 (1), 135–148.

Scharien, R.K., Hochheim, K., Landy, J., Barber, D.G., 2014. First-year sea ice melt pond fraction estimation from dual-polarisation C-band SAR–part 2: scaling in situ to Radarsat-2. Cryosphere 8 (6), 2163–2176.

Sturm, M., Holmgren, J., Perovich, D.K., 2002. Winter snow cover on the sea ice of the Arctic Ocean at the Surface Heat Budget of the Arctic Ocean (SHEBA): temporal evolution and spatial variability. J. Geophys. Res. Oceans 107 (C10).

Ulaby, F.T., Stiles, H.W., Abdelrazik, M., 1984. Snowcover influence on backscattering from terrain. IEEE Trans. Geosci. Remote Sens. GE-22 (2), 126–133.

Wang, Z., Schaaf, C.B., Chopping, M.J., Strahler, A.H., Wang, J., Roman, M.O., Shuai, Y., 2012. Evaluation of Moderate-resolution Imaging Spectroradiometer (MODIS) snow albedo product (MCD43A) over tundra. Remote Sens. Environ. 117, 264–280.

Wanner, W., Strahler, A.H., Hu, B., Lewis, P., Muller, J.P., Li, X., Barnsley, M.J., 1997. Global retrieval of bidirectional reflectance and albedo over land from EOS MODIS and MISR data: theory and algorithm. J. Geophys. Res. Atmos. 102 (D14), 17143–17161.

Webster, M.A., Rigor, I.G., Nghiem, S.V., Kurtz, N.T., Farrell, S.L., Perovich, D.K., Sturm, M., 2014. Interdecadal changes in snow depth on Arctic sea ice. J. Geophys. Res. Oceans 119 (8), 5395–5406.

Wiscombe, W.J., Warren, S.G., 1980. A model for the spectral albedo of snow. I: pure snow. J. Atmos. Sci. 37 (12), 2712–2733.

Yackel, J.J., Barber, D.G., 2000. Melt ponds on sea ice in the Canadian Archipelago: 2. On the use of RADARSAT-1 synthetic aperture radar for geophysical inversion. J. Geophys. Res. Oceans 105 (C9), 22061–22070.

Yackel, J.J., Barber, D.G., 2007. Observations of snow water equivalent change on landfast first-year sea ice in winter using synthetic aperture radar data. IEEE Trans. Geosci. Remote Sens. 45 (4), 1005–1015.

Yackel, J.J., Barber, D.G., Papakyriakou, T.N., Breneman, C., 2007. First-year sea ice spring melt transitions in the Canadian Arctic Archipelago from time-series synthetic aperture radar data, 1992–2002. Hydrol. Process. 21 (2), 253–265.